

# Direct Operando Visualization of Metal Support Interactions Induced by Hydrogen Spillover During CO<sub>2</sub> Hydrogenation

Kellie Jenkinson, Maria Chiara Spadaro, Viktoria Golovanova, Teresa Andreu, Joan Ramon Morante, Jordi Arbiol,\* and Sara Bals\*

The understanding of catalyst active sites is a fundamental challenge for the future rational design of optimized and bespoke catalysts. For instance, the partial reduction of Ce<sup>4+</sup> surface sites to Ce<sup>3+</sup> and the formation of oxygen vacancies are critical for CO<sub>2</sub> hydrogenation, CO oxidation, and the water gas shift reaction. Furthermore, metal nanoparticles, the reducible support, and metal support interactions are prone to evolve under reaction conditions; therefore a catalyst structure must be characterized under operando conditions to identify active states and deduce structure-activity relationships. In the present work, temperature-induced morphological and chemical changes in Ni nanoparticle-decorated mesoporous CeO<sub>2</sub> by means of in situ quantitative multimode electron tomography and in situ heating electron energy loss spectroscopy, respectively, are investigated. Moreover, operando electron energy loss spectroscopy is employed using a windowed gas cell and reveals the role of Ni-induced hydrogen spillover on active Ce<sup>3+</sup> site formation and enhancement of the overall catalytic performance.

## 1. Introduction

The chemical conversion with green hydrogen of the environmentally-problematic CO<sub>2</sub> molecule to CH<sub>4</sub> creates fundamental building blocks for carbon valorization on the industrial scale.<sup>[1,2]</sup> Metal oxide supports were originally implemented to stabilize small nanoparticles (NPs) from sintering, however supports are now understood to contribute more directly in catalysis via metal support interactions (MSI) such as charge transfer (CT), interface alloying or strong MSIs such as support overlayer formation, all of which provide powerful tools for catalyst optimization and bespoke catalyst design.<sup>[3,4,5]</sup> For instance, the choice in support material has been shown to be as important to determining the mechanism for CO<sub>2</sub> hydrogenation as the choice in precious metal catalyst.<sup>[6,7]</sup> Non-reducible supports (Al<sub>2</sub>O<sub>3</sub> and SiO<sub>2</sub>) preferably

perform the dissociative CO<sub>2</sub> reduction mechanism via CO where the entire hydrogenation reaction is restricted to the NP surface (summarized in **Figure 1**).<sup>[7]</sup> In contrast, CeO<sub>2</sub> is capable of promoting the formate pathway through Ce<sup>3+</sup> active sites and the corresponding oxygen vacancies which are known active sites for methane steam reforming, water gas shift (WGS) reaction and nitric oxide dissociation within automobile exhausts.<sup>[8,9]</sup> Ce<sup>3+</sup> sites are particularly desirable as CO<sub>2</sub> preferentially binds to Ce<sup>3+</sup> (Lewis base sites), activating the CO<sub>2</sub> molecule for bond breaking through an associative and energetically favorable route during the hydrogenation reaction in addition to extending the potential reaction area to the metal, reduced support, and NP-support interface (**Figure 1b**).<sup>[8,10,11]</sup>

Ce<sup>3+</sup> formation can be achieved under mild conditions through a NP mediated hydrogen spillover mechanism where H<sub>2</sub> dissociatively adsorbs on the NP before migrating to the support structure (**Figure 1a**).<sup>[12]</sup> This mechanism has been studied through in situ spectroscopy and to a lesser extent by environmental transmission electron microscopy (ETEM).<sup>[9,13,14,15]</sup>

Catalyst characterization under operando conditions has become a modern day, fundamental necessity to ascertain structure-property relationships of realistic catalysts.<sup>[16,17,18,19,20]</sup> This is because of the realization that NPs can dynamically change during a chemical reaction, and that the active state of the catalyst may be generated and only exist during the reaction. The dynamic evolution of active sites is as relevant and as likely in the


K. Jenkinson, S. Bals  
EMAT and NANOLab Center of Excellence  
University of Antwerp  
Antwerp 2020, Belgium  
E-mail: sara.bals@uantwerpen.be

M. C. Spadaro, J. Arbiol  
Catalan Institute of Nanoscience and Nanotechnology (ICN2)  
CSIC and BIST  
Campus UAB, Bellaterra, Barcelona, Catalonia 08193, Spain  
E-mail: arbiol@icrea.cat

V. Golovanova, T. Andreu, J. R. Morante  
IREC  
Jardins de les Dones de Negre 1, Sant Adrià del Besòs, Barcelona 08930,  
Spain

T. Andreu, J. R. Morante  
Institute of Nanoscience and Nanotechnology (IN2UB)  
Universitat de Barcelona  
Martí i Franquès, 1-11, Barcelona 08028, Spain

J. Arbiol  
ICREA  
Pg. Lluís Companys 23, Barcelona, Catalonia 08010, Spain

 The ORCID identification number(s) for the author(s) of this article can be found under <https://doi.org/10.1002/adma.202306447>

© 2023 The Authors. Advanced Materials published by Wiley-VCH GmbH. This is an open access article under the terms of the Creative Commons Attribution License, which permits use, distribution and reproduction in any medium, provided the original work is properly cited.

DOI: 10.1002/adma.202306447

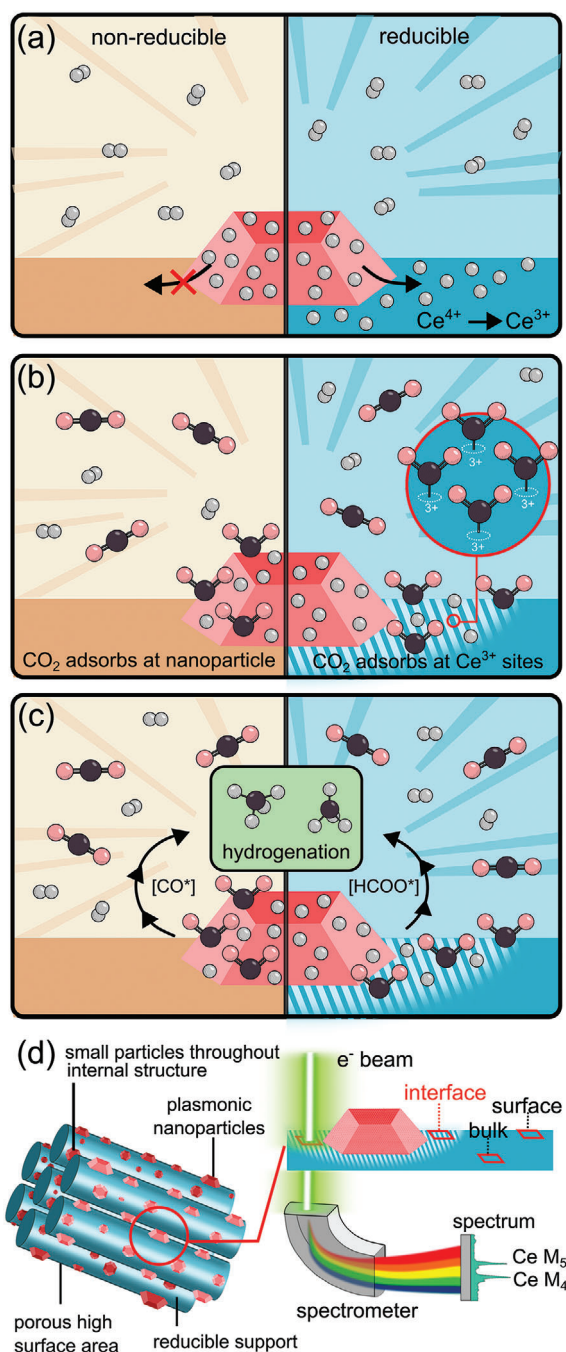


**Figure 1.** Illustrations highlighting fundamental differences between CO<sub>2</sub> hydrogenation on reducible and non-reducible supports and method to study spillover on a complex catalyst. a) Reducible supports facilitates hydrogen spillover from the Ni nanoparticle to CeO<sub>2</sub> resulting in partial Ce<sup>4+</sup> reduction to Ce<sup>3+</sup> possibly localized to the area surrounding the nanoparticle. b) Unlike the non-reducible support, for the CeO<sub>2</sub> support, CO<sub>2</sub> will preferentially bind to Ce<sup>3+</sup> sites localized at the NP-support interface. c) CO<sub>2</sub> hydrogenation on non-reducible supports is restricted to the Ni nanoparticle in the absence of support-based defect sites. For reducible supports, CO<sub>2</sub> molecules are concentrated at the Ni interface by Ce<sup>3+</sup> sites creating a reservoir of substrate molecules ideally situated for further hydrogenation. d) Illustration of complex mesoporous catalyst and operando electron energy loss spectroscopy technique to distinguish between Ce<sup>3+</sup> active sites at the surface, bulk, and metal–support interface.

support material as the supported NP, albeit support dynamics are comparatively seldom studied. Bulk scale operando spectroscopy studies have ascertained that Ce<sup>3+</sup> active sites, initially introduced through H<sub>2</sub> pretreatments, are generally reduced in abundance or entirely reoxidized during CO<sub>2</sub> hydrogenation, WGS and CO oxidation reactions.<sup>[8,16,21,22]</sup>

Although a catalyst's performance can be directly correlated with the abundance of Ce<sup>3+</sup> sites,<sup>[8]</sup> identifying and locating the active sites within a catalyst cannot be achieved by bulk-scale spectroscopy. As a result, locating active sites within heterogeneous catalysts has been identified as a fundamental knowledge gap and the latest challenge shared by microscopy and catalysis communities.<sup>[23,24]</sup> Gas-phase electron microscopy studies represent the forefront of operando investigations, providing single-particle and subnanometer resolutions necessary to distinguish between different surface sites (Figure 1d), and locate those sites sufficiently close to the supported NP to enable reagent interaction and contribute to the reaction.<sup>[16]</sup> Very recently, the impact of TiO<sub>2</sub> as a reducible support for CO<sub>2</sub> hydrogenation showed the evolution of strong MSI overlayers under reaction conditions using operando electron microscopy to identify the active catalyst–support dynamic and explain activity and selectivity trends.<sup>[25]</sup> However, there is a lack of equivalent operando electron microscopy studies where Ce<sup>3+</sup> active sites are the focus.

In this study, we investigate the structural and valency evolution of a mesoporous (MP) CeO<sub>2</sub> nanofiber assembly as a reducible support in a realistic and complex Ni/MP-CeO<sub>2</sub> catalyst using in situ and operando electron microscopy characterization in 2D and 3D. Ni/MP-CeO<sub>2</sub> was chosen due to the MP support maximizing opportunities for MSIs which likely facilitates the formate pathway and minimizing spatial constraints for Ni-bound H and Ce<sup>3+</sup>-bound CO<sub>2</sub> to promote reactant interaction, in addition to the use of plasmonic Ni NPs (2.4 x more active upon light irradiation),<sup>[10]</sup> all of which reflect modern concepts in advanced catalyst design in contrast to simplified model-like catalyst system (Figure 1d). By directly observing the catalyst during hydrogenation using electron microscopy, we aim to identify the location of active sites formed dynamically during the reaction to understand how reducible supports facilitate the formate pathway for CO<sub>2</sub> hydrogenation.

## 2. Results

### 2.1. In Situ Ni Nanoparticle Redistribution in 3D

Ni NPs (5–50 nm) dispersed on a mesoporous (MP) CeO<sub>2</sub> support, consisting of a templated assembly of CeO<sub>2</sub> nanofibers, was used as the realistic catalyst in this study.<sup>[10]</sup> The catalyst's thermal stability and NP mobility was investigated through an in situ heating HAADF-STEM tomography and EDX tomography experiment under ultra-high-vacuum (UHV) conditions. **Figure 2a** shows a low magnification HAADF-STEM image of a sufficiently small fragment of the Ni/MP-CeO<sub>2</sub> nanocomposite used for the tomography experiments. The CeO<sub>2</sub> nanofiber assembly is already apparent at this magnification with additional brightness-contrast that is likely due to the Ni NPs occupying the surface. However, with the complex variation in NP thickness due to the mesoporous structure and roughness of the individual CeO<sub>2</sub> nanofiber surface, the distribution of the Ni NPs is not easily

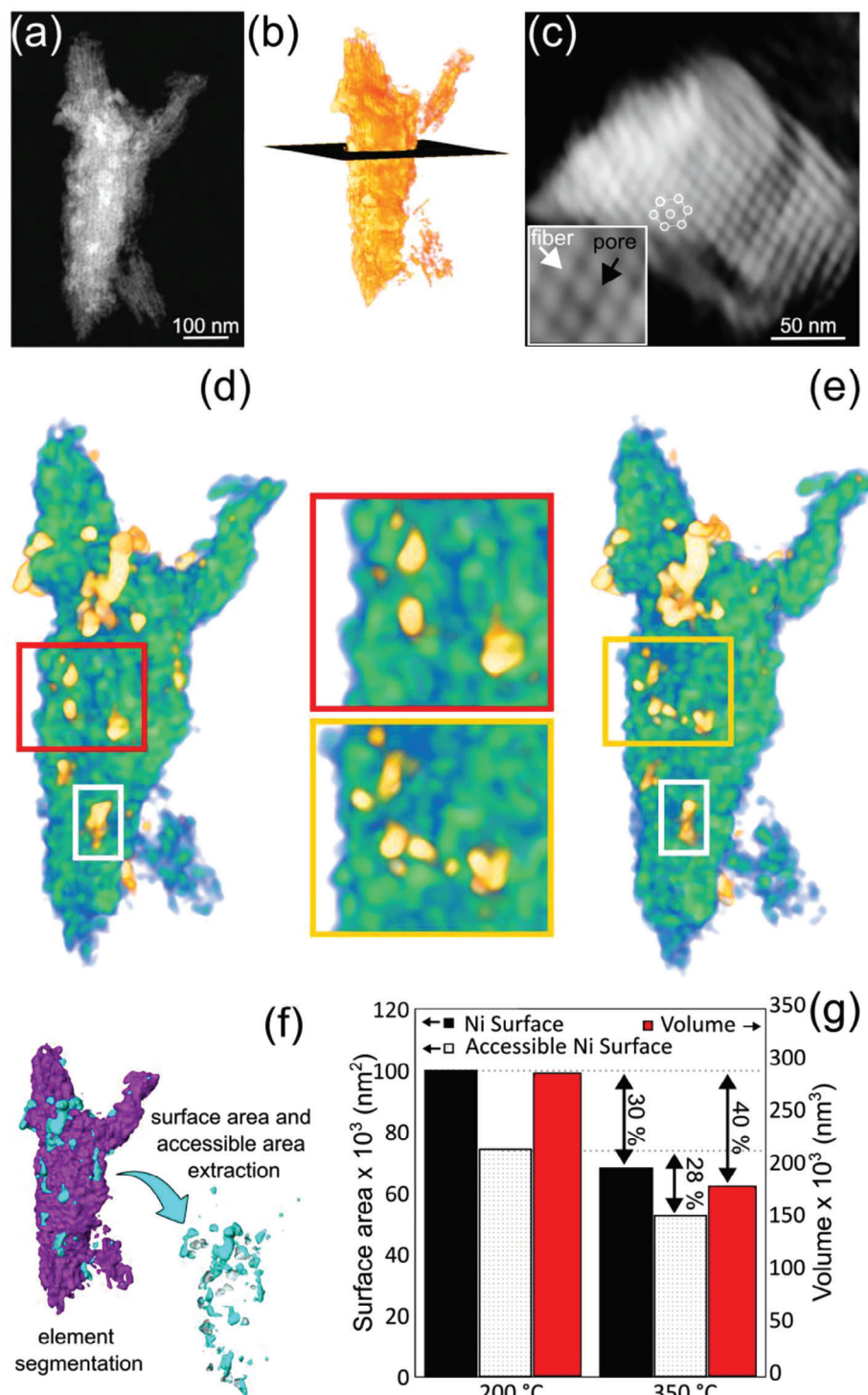


**Figure 2.** In situ multimode electron tomography of Ni/MP-CeO<sub>2</sub> catalyst. a) High angular annular dark field-scanning transmission electron microscopy (HAADF-STEM) image of catalyst fragment. b) HAADF electron tomography reconstruction showing the location of the slice through the volume, displayed in (c). c) Slice through the volume of the HAADF-STEM tomography reconstruction showing the internal structure of the mesoporous support. White overlay illustration shows the hexagonal packing arrangement of the fibers enforced through templating. c, inset) Magnified region from a part of the same slice where black and white arrows indicate a pore and nanofiber, respectively. d) EDX tomography reconstruction of the catalyst before thermal treatment (Ni = yellow, Ce = green). ROI highlighted by a red square is magnified to the right of the reconstruction. e) EDX tomography reconstruction of the same catalyst after thermal treatment (Ni = yellow, Ce = green). The ROI highlighted by a yellow square is magnified to the left of the reconstruction. f) Illustration of the segmentation process and accessible surface area calculation. g) 3D quantification of the surface area of Ni, accessible surface area of Ni, and volume of Ni before and after thermal treatment.

interpreted by the 2D HAADF-STEM brightness-contrast. HAADF-STEM tomography (Figure 2b,c) shows that the CeO<sub>2</sub> nanofibers are assembled into a hexagonal close packed arrangement and the diameter of the CeO<sub>2</sub> nanofiber and the approximate pore size was 6.75 ± 0.53 nm and 2.54 ± 0.26 nm, respectively (see Figure S1 in the Supporting Information). The EDX tomography reconstruction of the fragment (Figure 2d) shows Ni NPs (yellow) dispersed along the surface of the ceria assembly. The Ni NPs range in size from 50 nm, which would be restricted to surface occupation, to 1 nm which are sufficiently small to be able to reside within CeO<sub>2</sub> porous network.

Next, the catalyst was heated in situ to 350 °C for 15 min before quenching and the same region of interest (ROI) was investigated using a previously developed in situ heating tomography technique.<sup>[26]</sup> The EDX tomography reconstruction of the heated catalyst (Figure 2e) shows no evidence of nanofiber sintering or loss of fragment morphology. In contrast, the Ni NPs have fragmented to create smaller NPs. The same regions of Figure 2d,e are highlighted to show eight clearly defined and smaller separate NPs whereas the same region before heating only shows five. Similar NP division is seen throughout the reconstruction and highlighted by white rectangles to show NPs that are beginning to divide to produce two separate NPs. Several additional regions were monitored before and after heating without tomography acquisition to confirm the lack of NP sintering without prolonged electron beam exposure (Figures S2–S4, Supporting Information). The ability to transition from qualitative to quantitative characterization is an intrinsic advantage of investigating catalysts in 3D. Using the EDX tomography reconstructions before and after heating, the Ni and Ce surfaces were segmented to identify the change in Ni surface area (SA) and volume. Moreover, quantifying the interface between Ni NPs and the Ce support, the quantity of Ni surface accessible to substrate molecules can also be measured (Figure 2f,g and Figure S5, Supporting Information). Surprisingly, the Ni SA and accessible SA of the Ni residing on the outside of the CeO<sub>2</sub> assembly is reduced by 32% and 30% respectively. This reduction in SA initially seems counter-intuitive as the NPs are increasing in number and becoming smaller. However, slices taken from the EDX reconstruction (Figure S6, Supporting Information) before and after heat treatment show that there is an increase in Ni signal and evidence of well-defined NPs within the porous structure. This restricted Ni size within the MP-CeO<sub>2</sub> pores poses limitations for direct visualization, interaction volume, and X-ray generation to locate subsurface Ni NPs except for the very largest NPs identified by arrows in Figure S6 (Supporting Information). The volume loss of almost 40% after heating suggests a far larger loss in volume compared to surface area loss (30%). This demonstrates that although there is a large volume of Ni translated into the pores, the particles that can be visualized at the surface have a net increase in SA due to NP fragmentation.

## 2.2. In Situ Electron Energy Loss Spectroscopy

Electron energy loss spectroscopy (EELS) was used to measure distribution and abundance of Ce<sup>3+</sup> during thermal treatment under catalytically relevant temperatures under UHV conditions. The Ce M<sub>4,5</sub> ionization edge was used as the edges are

sharp, easily resolved, and the fine structure provides Ce valency information.<sup>[27]</sup> Figure 3a–c shows EEL spectra compared from the near and far regions with respect to the Ni NP to reveal no variation in Ce oxidation state based on proximity to Ni NPs (Figure 3b). During this acquisition, the catalyst was heated to 120 °C to minimize carbon contamination while EELS maps were acquired. EELS measurements acquired at room temperature, before contamination prevented further investigation, confirms that there is no change in Ce valency by heating to this relatively low temperature compared to the high temperature annealing conditions (Figure S7, Supporting Information). Ce oxidation state indifference to Ni proximity within the pristine catalyst can be seen also in Figure 3d,e.

Valency mapping during in situ heating (Figure 3d–f and Figure S8, Supporting Information) revealed that Ce<sup>3+</sup> abundance does not increase at elevated temperatures and still remains independent to Ni proximity at 400 °C. Moreover, the stability of EELS peak-intensity, energy resolution and energy shift of both Ni and Ce ionization edges are unchanged within the RT – 400 °C temperature range.

## 2.3. Operando CO<sub>2</sub> Hydrogenation

The Ce<sup>3+</sup> abundance and distribution under operando CO<sub>2</sub> hydrogenation conditions was investigated using a windowed gas cell and an online gas analyzer to confirm the formation of methane (Figure S9, Supporting Information). EELS maps were taken from several ROI of the Ni/MP-CeO<sub>2</sub> catalyst at 200 °C in an inert He environment (Figure 4a–c,e). The Ce<sup>3+</sup> abundance was measured at 8% of the overall Ce signal and is evenly distributed throughout the support structure. The quantity and distribution are consistent with equivalent in situ heating EELS measurement in UHV conditions and shows that, when under atmospheric pressure, Ce<sup>3+</sup> does not arbitrarily form in the absence of CO<sub>2</sub> and H<sub>2</sub>. The temperature was elevated to 350 °C and CO<sub>2</sub> and H<sub>2</sub> gases were introduced in the stoichiometric ratio, optimal for CO<sub>2</sub> hydrogenation to methane (70% He, 24% H<sub>2</sub>, 6% CO<sub>2</sub>, 1 Bar). The catalyst was left for ≈1 h under hydrogenation conditions to allow the holder to stabilize from temperature and pressure changes. During this time, the electron beam was blanked to prevent additional and unnecessary electron beam irradiation. EELS mapping of the same ROI shown in Figure 4a–c was measured under CO<sub>2</sub> hydrogenation conditions (Figure 4f,g) and shows a clear increase in Ce<sup>3+</sup> abundance with the overall Ce<sup>3+</sup> percentage increasing from 8% to 18%. The increase in Ce<sup>3+</sup> abundance under hydrogenation conditions is a consistent observation over several catalyst fragments in addition to control regions where the fragment was not previously measured to ensure that Ce<sup>3+</sup> formation is not due to electron beam-induced artefacts (Figures S10–S13, Supporting Information). EEL spectra of two regions within the measured area have been extracted and shown in Figure 4d alongside reference spectra for Ce<sup>3+</sup> and Ce<sup>4+</sup>. The Ce EEL spectrum taken from CeO<sub>2</sub> residing at the surface of the Ni NP shows a clear broadening of Ce M<sub>4,5</sub> ionization edge in addition to a shift to lower energy compared to the Ce signal extracted from the bulk support indicating a significant location-specific reduction of Ce<sup>4+</sup> to Ce<sup>3+</sup>. The abundance of Ce<sup>3+</sup> at these two regions equals 23% and 13%

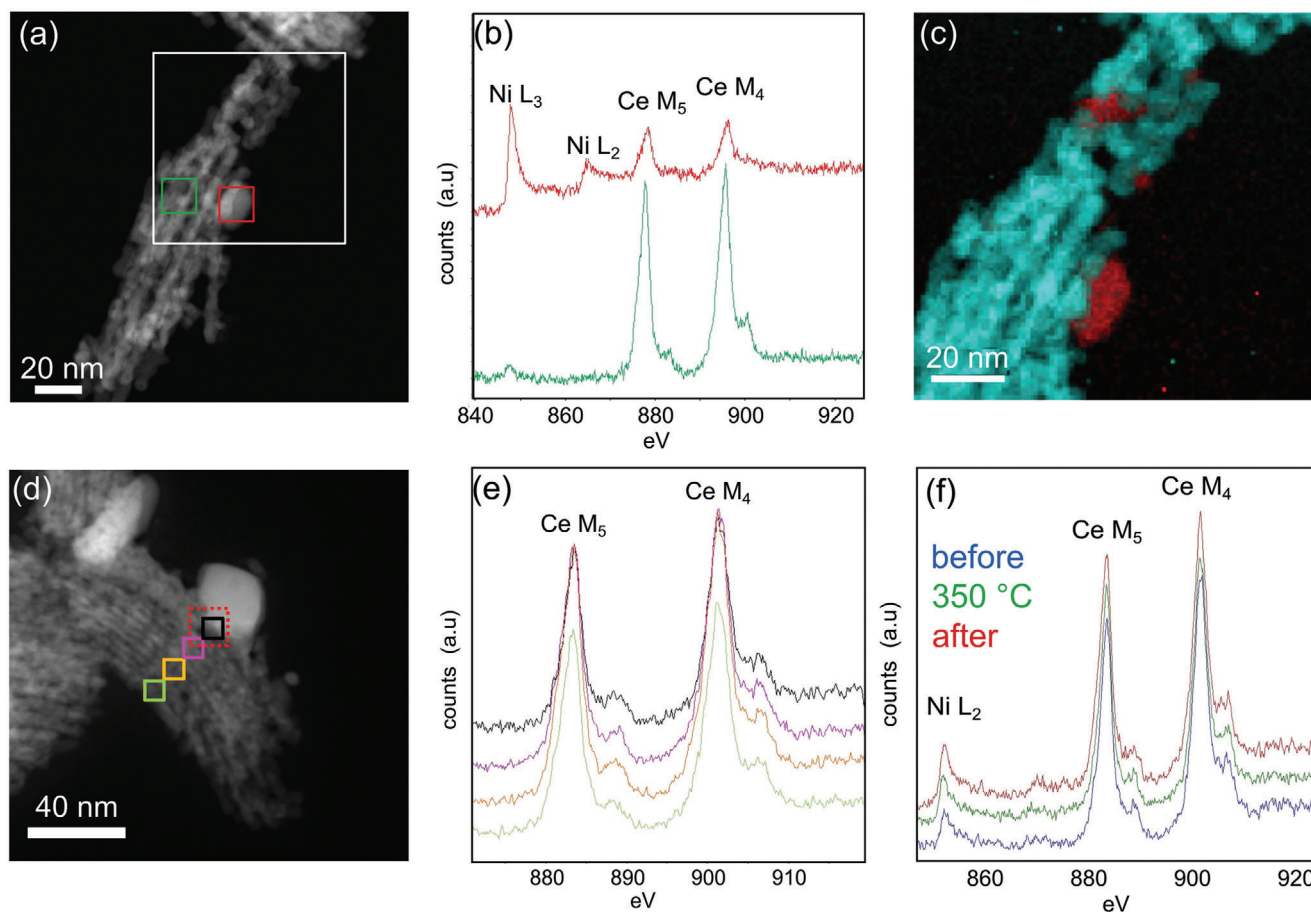


**Figure 3.** In situ electron energy loss spectroscopy and high angular annular dark field-scanning transmission electron microscopy (HAADF-STEM) micrographs of Ni/MP-CeO<sub>2</sub> catalyst during thermal treatment in ultra-high vacuum conditions. a) ROI 1 HAADF STEM image of Ni/MP-CeO<sub>2</sub> fragment at 120 °C, white box indicates the mapping area and red and green boxes indicate the location of spectra extracted in (b). b) EEL spectra of two areas within ROI 1, close to the Ni NP (red) and far from the Ni NP (green). c) elemental distribution of Ni (red) and Ce (blue) extracted from EELS mapping. d) HAADF-STEM image of Ni/MP-CeO<sub>2</sub> fragment (ROI 2). Solid boxes indicate the location of spectra extracted in e and the dashed box indicates the location of spectra extracted in (f). e) Extracted EEL spectra of four locations at increasing distance from Ni NP shown in d at 120 °C. f) Extracted EEL spectra of the same location before (blue), during (green), and after (red) heating to 400 °C. Location of spectrum extraction is identified in (d) by a dashed red box.

for surface and bulk regions respectively. Figure 4h shows line scan intensity profiles for the Ce<sup>3+</sup> and Ce<sup>4+</sup> signals over the CeO<sub>2</sub> structure. The line scan profile shows a clear core@shell structure with Ce<sup>3+</sup> preferentially occupying the surface of the individual CeO<sub>2</sub> nanofibers that make up the larger CeO<sub>2</sub> mesoporous structure. Furthermore, the depth of the reduced surface within the individual CeO<sub>2</sub> fibers is consistent, however the abundance in Ce<sup>3+</sup> at the surface of each fiber increases significantly with proximity to the NP. Of the four fibers within the field of view, the reduced surface increases from 12% for the nanofiber furthest away from Ni, to 17%, 28% and finally 45% for the nanofiber supporting the Ni NP.

The operando EELS experiment was extended to consider a broader range of reaction temperatures (200–400 °C). Figure 4i,j shows the elemental distribution of Ni and Ce in addition to a Ce<sup>3+</sup> valency map for an alternative fragment under inert conditions (He) at 200 °C. The initial Ce<sup>3+</sup> abundance was 6% distributed evenly over the fragment. Figure 4k shows an increase in Ce<sup>3+</sup> concentration at the surface of the CeO<sub>2</sub> support and

an overall Ce<sup>3+</sup> increase to 11% under hydrogenation conditions which is further increased to 16% when increasing the temperature to 400 °C (Figure 4l). Evidence of a location selective lack of reduction was also observed at locations where the Ni NPs reside which are highlighted by white arrows in Figure 4l.

### 3. Discussion

Thermally-induced sintering is a fundamental deactivation mechanism for supported NP catalysts, both due to the loss of NP surface area and the loss of NP-support interfaces. To study Ni dispersion, mobility, sintering, and to quantify the loss of NP surface area and interfaces within the mesoporous structure, 3D analysis is crucial. 3D studies under gaseous conditions are uniquely challenging to achieve as windowed gas cells lack the angular range necessary for tomography, ETEM tomography's limited environmental pressures is more akin to a reduced vacuum than atmospheric pressure, and atom counting reconstructions from 2D datasets have not been applied to such

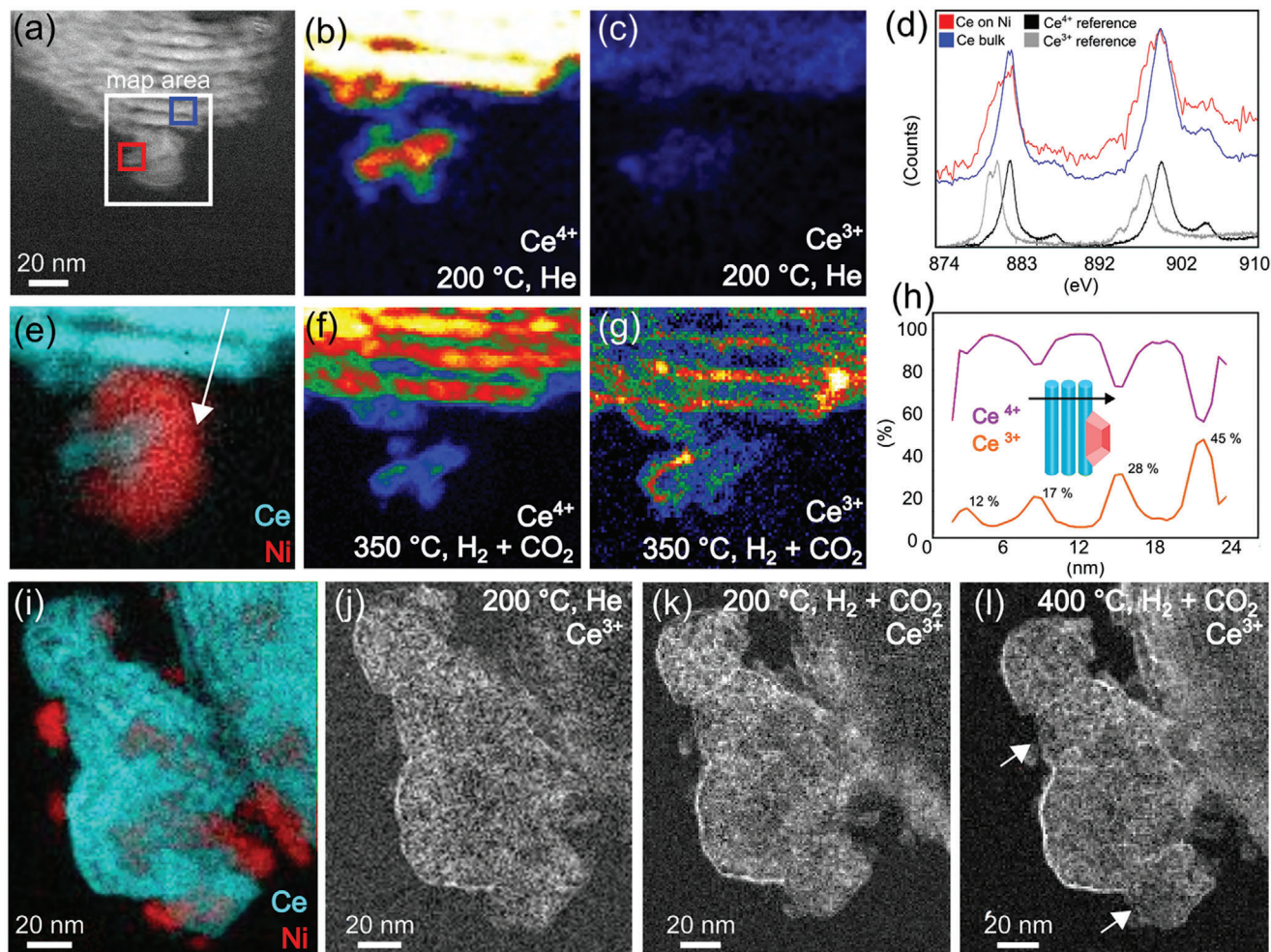


**Figure 4.** Operando electron energy loss spectroscopy (EELS) of Ni/MP-CeO<sub>2</sub> under hydrogenation conditions. a) high angular annular dark field-scanning transmission electron microscopy (HAADF-STEM) image of a catalyst fragment indicating the mapping area (white box) and locations for spectra extraction for CeO<sub>2</sub> residing on the Ni NP and further away from Ni NP (red and blue boxes respectively). b,c) Ce<sup>4+</sup> and Ce<sup>3+</sup> spectral intensity maps to reflect the presence and abundance of that valence state for the catalyst fragment shown in (a), heated at 200 °C in He. d) EEL spectra of CeO<sub>2</sub> region residing on the Ni NP (red box in a) and further away from Ni NP (blue box in a) at 350 °C under hydrogenation conditions compared to reference EEL spectra for Ce<sup>3+</sup> and Ce<sup>4+</sup>. e) Elemental maps for Ni (red) and Ce (blue). The white arrow indicates the location and direction of the line scan extraction shown in (h). f,g) Ce<sup>4+</sup> and Ce<sup>3+</sup> spectral intensity maps to reflect the presence and abundance of that valence state for the catalyst fragment shown in (a), heated at 350 °C in hydrogenation conditions. h) Ce<sup>3+</sup> (orange) and Ce<sup>4+</sup> (purple) intensity line scan profiles from the location identified in (e). i) Elemental maps for Ni (red) and Ce (blue) extracted from EELS signals of a second Ni/MP-CeO<sub>2</sub> fragment. j) Ce<sup>3+</sup> spectral intensity map for the catalyst fragment shown in (i), heated at 200 °C in He. k) Ce<sup>3+</sup> spectral intensity map for the catalyst fragment shown in (i), heated at 200 °C in hydrogenation conditions. l) Ce<sup>3+</sup> spectral intensity map for the catalyst fragment shown in (i), heated at 400 °C in hydrogenation conditions. White arrows highlight the lack of Ce<sup>3+</sup> at the locations of Ni NPs.

large and complex architectures.<sup>[28–30]</sup> Therefore the catalyst's thermal stability and NP mobility was investigated through an in situ heating HAADF-STEM tomography under UHV conditions. The acquisition was combined with EDX tomography as it was not possible to assess Ni distribution by brightness contrast due to HAADF-STEM projections having a significant contribution from both thickness contrast and Z contrast. Although UHV conditions do not directly translate to reaction conditions during CO<sub>2</sub> hydrogenation, the designed experiment enables a quantitative assessment of the influence of temperature separately, which can be incorporated into the 2D operando measurements.

The in situ thermal annealing studies conducted in 3D using electron tomography confirm that the CeO<sub>2</sub> mesoporous structure maintains its hexagonal close packed nanofiber arrangement (Figure S14, Supporting Information). Contradictory to the expected Ni sintering behavior, the Ni NPs fragment to produce a larger number of smaller NPs in addition to a significant translation of ≈40% Ni volume into the porous structure. The Ni NPs fragmenting and translating into the porous network with a restrictive pore diameter will enforce a dispersion of small (< 2.5 nm) NPs at elevated temperatures which is a recognized method to prepare small Ni NPs from larger parent NPs.<sup>[31]</sup> Therefore, our in situ thermal treatment of Ni/MP-CeO<sub>2</sub> shows

that the catalyst evolves under catalytically relevant temperatures to enhance the quantity of NP-support interfaces necessary to generate  $\text{Ce}^{3+}$  active sites and boost activity.

To investigate  $\text{Ce}^{3+}$  active site formation under operando conditions, one must distinguish between hydrogen spillover during catalysis from other potential MSIs such as charge transfers (CT) induced by Ni deposition or thermal treatment.<sup>[32]</sup> EELS mapping of several pristine Ni/MP-CeO<sub>2</sub> fragments show an overall  $\text{Ce}^{3+}$  composition of  $\approx 8\%$  which is uniformly distributed throughout the CeO<sub>2</sub> structure, therefore ruling out CT at the Ni-Ce interface during Ni deposition. In situ heating EELS mapping of several Ni/MP-CeO<sub>2</sub> fragments also showed a consistent  $\text{Ce}^{3+}$  abundance throughout the CeO<sub>2</sub> mesoporous structure and at the Ni-Ce interface showing that CT MSIs were not induced under catalytically relevant temperatures without hydrogen or CO<sub>2</sub> hydrogenation conditions. Therefore, we can expect any valency changes under CO<sub>2</sub> hydrogenation conditions to be a consequence of catalyst-substrate interactions as we have established that thermal treatment does not induce any change within Ce oxidation state. Moreover, these in situ heating EELS investigations confirm that  $\text{Ce}^{3+}$  is not artificially generated by electron beam-induced artefacts during map acquisition at elevated temperatures as there were no observed electron beam-induced morphology, structural, or valency changes during multiple successive acquisitions.

In situ heating experiments have proven the thermal stability of both the Ni NPs decorating the porous structure and Ce oxidation state in the absence of H<sub>2</sub> and CO<sub>2</sub> exposure. In order to investigate the role of reaction gases on the morphological and chemical structure of the catalyst, we performed a similar study under catalytically relevant CO<sub>2</sub> hydrogenation conditions. In the majority of bulk scale operando studies, the extent of  $\text{Ce}^{3+}$  sites available are initially introduced by a reductive annealing pretreatments followed by their partial destruction or reoxidation during reaction conditions.<sup>[8,16,21,22]</sup> However, the ability of a catalyst to favor the formate pathway of CO<sub>2</sub> hydrogenation is not a product of additional reductive annealing pretreatments, rather it is an intrinsic property of the catalyst material.<sup>[7]</sup> Therefore, in this study, the ability of Ni/MP-CeO<sub>2</sub> to form CeO<sub>2</sub>-based active sites under operando conditions was investigated without preheating in H<sub>2</sub>. The operando CO<sub>2</sub> hydrogenation experiment summarized in Figure 4, shows an increased abundance in  $\text{Ce}^{3+}$  active site formation selectively at the CeO<sub>2</sub> nanofiber surface upon CO<sub>2</sub> hydrogenation at 350 °C. The resulting active catalyst consists of an assembly of CeO<sub>2</sub> nanofibers displaying a core@shell arrangement with a partially reduced shell. The  $\text{Ce}^{3+}$  active site formation occurs preferentially in close proximity to Ni NPs with the highest  $\text{Ce}^{3+}$  abundance found at the CeO<sub>2</sub> support directly interfacing with Ni. The increased number of  $\text{Ce}^{3+}$  active sites at the catalyst surface boosts the CO<sub>2</sub> binding and hydrogenation through the associative route.

The operando EELS measurements show that hydrogen spillover under hydrogenation conditions was not limited to the nanofiber interfacing with the Ni NP, rather hydrogen was found to traverse the complex mesoporous network over tens of nanometers to reduce the surface of neighboring CeO<sub>2</sub> nanofibers owed to CeO<sub>2</sub> proton conductivity.<sup>[33]</sup> Interestingly, the depth of the reduced surface within the individual CeO<sub>2</sub> fibers is consistent ( $\approx 2$  nm), however the abundance in  $\text{Ce}^{3+}$  at the sur-

face of each nanofiber increases significantly with proximity to the NP. Of the four fibers within the field of view,  $\text{Ce}^{3+}$  shell abundance increases from 12% for the nanofiber furthest away from Ni, to 17%, 28%, and finally 45% for the nanofiber supporting the Ni NP.

Following the high  $\text{Ce}^{3+}$  concentrations measured at 350 °C, CO<sub>2</sub> hydrogenation was repeated over a broader range of temperatures (200–400 °C) to reflect those typically used in heterogeneous catalysis.<sup>[10]</sup> Remarkably, even mild reaction conditions (200 °C) shows a surface selective  $\text{Ce}^{3+}$  active site formation in close proximity to the Ni NPs. Upon increasing the reaction temperature to 400 °C, the abundance of  $\text{Ce}^{3+}$  is increased further still. Interestingly, the depth of the surface selective reduction and the distance hydrogen spillover traverses the support surface from the Ni NP, does not appear to be influenced by temperature. In addition to a surface selective reduction, we also observe a location-selective absence of active site formation on the CeO<sub>2</sub> support directly occupied by the Ni NPs. This observation supports the hypothesis that  $\text{Ce}^{4+}$  reduction is due to a hydrogen spillover event rather than an alternate MSI such as CT as hydrogen is incapable of “spilling over” at the location occupied by Ni. In contrast, if  $\text{Ce}^{3+}$  active sites were formed through the Ni-Ce interface by CT, one would expect the Ce sites directly underneath the Ni NP to show the highest abundance of  $\text{Ce}^{3+}$ .

We show through operando electron microscopy that hydrogen spillover extends over the support surface by tens of nanometers, radiating from the Ni NP, and potentially explains the superior catalytic performance of the catalyst, which exhibit associative CO<sub>2</sub> hydrogenation pathways. The large area of  $\text{Ce}^{3+}$  active sites around the Ni NP, favoring the associative route, boosts CO<sub>2</sub> hydrogenation. In contrast, the dissociative pathway is restricted to the active area provided solely by the NP surface, as the carbonyl radicals bound preferably to the metallic NPs.

#### 4. Conclusion

To conclude, we have demonstrated that at typical CO<sub>2</sub> hydrogenation reaction temperatures, Ni/MP-CeO<sub>2</sub> is able to dynamically increase the surface area of the decorated NPs and increase the amount of Ni-Ce interfacial sites, by fragmentation and relocation of the Ni NPs, necessary to promote MSIs for enhanced performance. We also show that during relevant reaction temperatures, there are no metal support interactions such as a charge transfer processes between the Ni NP and reducible support structure which could impact the catalysts performance.

By tracking the formation and location of  $\text{Ce}^{3+}$  active sites during CO<sub>2</sub> hydrogenation, we show that hydrogen spillover occurs during the reaction and extends over tens of nanometers over the support surface, radiating from the Ni NP, at temperatures as low as 200 °C. Moreover, we observe that before the reaction a small amount of  $\text{Ce}^{3+}$  sites ( $<10\%$ ) is uniformly distributed throughout CeO<sub>2</sub>, while the spillover-induced Ce reduction occurs selectively at the surface of the support in close proximity to the Ni nanoparticle. The depth of  $\text{Ce}^{3+}$  formation from the support surface was determined to be independent of hydrogenation temperature, however the abundance of  $\text{Ce}^{3+}$  increases with reaction temperature. Furthermore, we show that hydrogen spillover is not limited to the CeO<sub>2</sub> nanofiber in direct contact with nickel nanoparticles and can traverse the nanofiber assembly making

up the mesoporous support. These results show that under CO<sub>2</sub> hydrogenation reaction conditions, the catalyst evolves further to generate dynamic Ce<sup>3+</sup> active sites located at the Ni/MP-CeO<sub>2</sub> interface and the surrounding support (over several nanometers) to directly boost catalytic performance and promote formate pathways. As the Ce<sup>3+</sup> active sites were dynamically formed during the reaction, working under operando conditions benefiting sub-nanometer resolutions was crucial to understand our active catalyst structure and to locate atomic-level active sites necessary to fuel future catalyst design.

## 5. Experimental Section

All in situ and operando electron microscopy studies were carried out using an aberration-corrected ThermoFisher Scientific – Titan Cubed electron microscope operating at 300 kV. The Ni/MP-CeO<sub>2</sub> catalyst was prepared by a previously reported method<sup>[10]</sup> and was dispersed in ethanol by sonication and drop cast (≈10 μL) on an appropriate MEMS chip.

**In Situ Heating Multimode Tomography:** In situ heating experiments were carried out on a dedicated heating holder (wildfire, DENS solutions) on a Si<sub>3</sub>N<sub>4</sub> MEMS chip. Several regions of interest (ROI) were imaged at room temperature to establish a baseline structure. Next, the temperature was increased to 200 °C to prevent the build-up of carbonaceous contamination and a HAADF and EDX tilt series were acquired using a 150 pA screen current (HAADF acquisition: 2° intervals ± 80°, EDX acquisition: 10° intervals ± 80°) using a Super-X detector. Several ROIs were imaged in 2D in addition to EDX maps to ensure that the catalyst did not change over a prolonged period of time at this temperature. In addition, 2D HAADF-STEM images were acquired before and after the tomography acquisition to ensure that the catalyst's structure had not been altered by the electron beam. Next, the temperature was increased to 350 °C for 15 min, during this time, an alternative window was monitored to prevent additional electron beam irradiation to the ROIs. The temperature was reduced to 200 °C and equivalent tilt series were acquired for the catalyst fragments after heat treatment. The resulting data was reconstructed using an expectation maximization (EM) reconstruction algorithm using a HAADF-STEM signal for accurate alignment. To extract Ni surface and accessible surface area relevant for catalysis, Ce and Ni phases were identified by segmentation of the EDX tomography reconstruction by selecting an appropriate threshold value using the Amira software. A triangular surface grid of both Fe and Au materials was generated from the previous segmentation step using 1024×1024×1024 3D voxel resolution to generate ≈14 000 000 triangles. As only a proportion of the Ni NPs at the surface are in contact with the support, one cannot subtract Ni's surface area from Ce's surface area. Rather, the Ni surface in contact with Ce must be calculated first, so that accurate accessible Ni surface areas could be derived. Using a surface generation module, boundary surfaces can be extracted and later removed for a final Ni surface area.

**In Situ Heating Scanning Transmission Electron Microscopy – Electron Energy Loss Spectroscopy (STEM-EELS):** In situ heating experiments were carried out on a dedicated heating holder (wildfire, DENS solutions) on a Si<sub>3</sub>N<sub>4</sub> MEMS chip. EELS and annular dark field (ADF) measurements were carried out using an aberration corrected ThermoFisher Scientific – Titan Cubed electron microscope, operating at 300 kV, equipped with an energy monochromator excited to a value of 0.7, and a screen current of 50 pA was used to limit the beam intensity and minimize potential beam-induced artefacts. The energy resolution provided by the electron monochromator, as measured from the full-width half maximum of acquired zero-loss peaks, was 0.2 eV. The dispersion of the spectrometer was set to 0.1 eV ch<sup>-1</sup> and 2000 channels are used to cover an energy range from 835 eV to 1040 eV, to visualize Ni L<sub>2,3</sub> and Ce M<sub>4,5</sub> ionization edges. The catalyst was heated to 120 °C to minimize carbon contamination while EELS maps were acquired. The temperature was increased to the target 350 °C for a high temperature annealing stage in ultra-high-vacuum conditions. The temperature was maintained for 15 minutes to allow the

holder to stabilize, during which time the electron beam was blanked to prevent unnecessary sample irradiation. Spectra were acquired at 350 °C in UHV conditions followed by a reduction in temperature to 120 °C for the final EELS acquisition.

**Operando Electron Energy Loss Spectroscopy:** Operando experiments were carried out using a windowed gas cell nanoreactor (climate G+, DENS solutions) comprising of two electron-transparent Si<sub>3</sub>N<sub>4</sub> windowed chips. Ni/MP-CeO<sub>2</sub> was dispersed in ethanol and deposited on the lower climate chip before constructing the climate holder and sealing the nanoreactor. The nanoreactor consists of a top and bottom chip of 50 nm and 30 nm thickness respectively. The internal temperature of the microreactor was accurately controlled by a 4-point probe method.

Similarly, to the in situ heating EELS experiments, measurements were carried out using an aberration corrected electron microscope operating at 300 kV equipped with an energy monochromator excited to a value of 0.7. The energy resolution provided by the electron monochromator, as measured from the full-width half maximum of acquired zero-loss peaks, was 0.2 eV. The dispersion of the spectrometer was set to 0.1 eV ch<sup>-1</sup> and 2000 channels are used to cover an energy range from 835 eV to 1040 eV, to visualize Ni's L<sub>2,3</sub> and Ce M<sub>4,5</sub> ionization edges. To minimize potential electron beam-induced artefacts, the electron dose was reduced to ≈5580 e<sup>-</sup> Å<sup>-2</sup> and a low screen current of 50 pA, which is consistent with previous in situ and gas phase STEM microscopy investigations.<sup>[22,25,29]</sup> All gas supply system lines and the nanoreactor were subject to a pump-purge protocol three times to flush any moisture and oxygen from the system. The gas lines and nanoreactor were flushed with inert He and the temperature increased to 200 °C to acquire EELS maps of several ROI under flowing He. The gas mixture was changed to 70% He, 24% H<sub>2</sub>, 6% CO<sub>2</sub> (1 Bar) which first passed through a mixing chamber to ensure a homogeneous gas mixture before introduction to the catalyst. The initial mixed gases were diverted from the chamber directly to the exhaust for 5 minutes until a homogeneous mixture was achieved. The temperature was increased to 350 °C and the well mixed He, H<sub>2</sub>, and CO<sub>2</sub> reactants were passed through the nanoreactor to mix with the catalyst and the outlet gas flow was connected to a gas analyzer (DENS solutions) to confirm CO<sub>2</sub> hydrogenation. The holder was left to stabilize from the temperature and pressure changes for one hour, during which time the electron beam was blanked to limit electron beam irradiation. EELS maps were acquired under flowing CO<sub>2</sub> and H<sub>2</sub> gases for several ROIs. New ROIs were also chosen from previously unexposed windows to confirm if Ce valency changes detected were not electron beam-induced artefacts. In a separate series of experiments, the procedure was repeated to investigate a broader temperature range and to confirm that our observed active site formation was reproducible. In this case, the nanoreactor was first flushed with He to acquire EELS maps of the pristine catalyst at 200 °C, followed by switching the gas mixture to 70% He, 24% H<sub>2</sub>, 6% CO<sub>2</sub> (1 bar) at a constant temperature (200 °C) for EELS map acquisitions at a lower reaction temperature. The procedure was then repeated at 400 °C to investigate a higher reaction temperature.

In addition to minimizing the electron beam intensity to prevent electron beam-induced artefacts, we also implemented additional measures to ensure the reliability of our results. For instance, we elected to blank the electron beam in between acquisitions and when the climate system was stabilizing from changing reaction parameters (temperature of gas feed mixture) to prevent unnecessary additional irradiation. Furthermore, to ensure that the catalyst's structural evolution was not a product of electron beam exposure, the observed catalyst behavior at key stages of the experiments with alternative windows that had no prior electron beam exposure was compared. This comparison method aligns with current state-of-the-art in situ microscopy studies of MSIs<sup>[25,34,35]</sup> and showed an identical Ce<sup>3+</sup> formation without additional irradiation, therefore allowing us to conclude that our observations are not a product of electron beam-induced artefacts.

**Ce<sup>3+</sup>/Ce<sup>4+</sup> Determination from Electron Energy Loss Spectroscopy:** The EEL spectra were acquired in the form of 2D spectral maps. Therefore, the EEL spectrum of each pixel within the 2D array can be extracted and the abundance of Ce<sup>3+</sup>/Ce<sup>4+</sup> calculated. In order to obtain the presence and strength of each valence state for Ce, a spectrum is extracted from



each pixel and fit to reference spectra by performing multiple linear least-squares (MLLS) fitting. The reference spectra used were obtained from bulk samples of  $\text{CeF}_3$  and  $\text{CeO}_2$  for  $\text{Ce}^{3+}$  and  $\text{Ce}^{4+}$ , respectively. The resulting quantification can be displayed in terms of signal strength such as “counts” for each Ce valence state within each pixel to generate a 2D valency map.<sup>[27,36]</sup> In the case where a percentage of  $\text{Ce}^{3+}/\text{Ce}^{4+}$  is stated instead of signal intensity (counts), this is achieved by summing the spectral maps to calculate an overall Ce signal intensity for a dedicated pixel or collection of pixels, followed by calculating how much of the total Ce signal is fitted to  $\text{Ce}^{3+}$  or  $\text{Ce}^{4+}$  displayed as a percentage value.

## Supporting Information

Supporting Information is available from the Wiley Online Library or from the author.

## Acknowledgements

K.J. and S.B. acknowledge funding from ERC Consolidator Grant #815128 – REALNANO and European Union’s Horizon 2020 research and innovation program under grant agreement #823717 – ESTEEM3. The authors want to acknowledge Dr. Wiebke Albrecht and Prof. dr. Thomas Altantzis for their contribution to discussions and initial experimentation. ICN2 and IREC acknowledge funding from Generalitat de Catalunya 2021SGR00457 and 2021SGR01581, respectively. This study is part of the Advanced Materials programme and was supported by MCIN with funding from European Union NextGenerationEU (PRTR-C17.11) and by Generalitat de Catalunya. The authors thank support from the projects PID2019-108136RB-C33, PID2020-116093RB-C42, and -C43, funded by MCIN/AEI/10.13039/501100011033/ and by “ERDF A way of making Europe”, by the “European Union”. ICN2 is supported by the Severo Ochoa program from Spanish MCIN / AEI (Grant No.: CEX 21-001214-S). ICN2 and IREC are funded by the CERCA Programme / Generalitat de Catalunya. This study was supported by EU HORIZON INFRA TECH 2022 project IMPRESS (Ref.: 101094299). IREC thanks support from H2020 MSCA CO-Fund 2016 program DOC-FAM. This study is part of the Advanced Materials programme and was supported by MCIN with funding from European Union NextGenerationEU (PRTR C17.11) and by Generalitat de Catalunya. The present work is a collaboration within e-DREAM.<sup>[37]</sup>

## Conflict of Interest

The authors declare no conflict of interest.

## Data Availability Statement

The data that support the findings of this study are available from the corresponding author upon reasonable request.

## Keywords

$\text{CO}_2$  hydrogenation, electron microscopy, heterogeneous catalysis, in situ, operando

Received: July 3, 2023

Revised: October 18, 2023

Published online: November 16, 2023

[1] W. Wang, S. Wang, X. Ma, J. Gong, *Chem. Soc. Rev.* **2011**, *40*, 3703.

- [2] C. Vogt, M. Monai, G. J. Kramer, B. M. Weckhuysen, *Nat. Catal.* **2019**, *2*, 188.
- [3] T. W. Van Deelen, C. Hernández Mejía, K. P. De Jong, *Nat. Catal.* **2019**, *2*, 955.
- [4] Y. Lykhach, S. M. Kozlov, T. Skála, A. Tovt, V. Stetsovych, N. Tsud, F. Dvořák, V. Johánek, A. Neitzel, J. Mysliveček, S. Fabris, V. Matolín, K. M. Neyman, J. Libuda, *Nat. Mater.* **2016**, *15*, 284.
- [5] S. Bernal, J. J. Calvino, M. A. Cauqui, J. M. Gatica, C. Larese, J. A. Pérez Omil, J. M. Pintado, *Catal. Today* **1999**, *50*, 175.
- [6] J. Guilera, J. Del Valle, A. Alarcón, J. A. Díaz, T. Andreu, *J. CO2 Util.* **2019**, *30*, 11.
- [7] M. Boaro, S. Colussi, A. Trovarelli, *Front Chem* **2019**, *7*.
- [8] F. Wang, S. He, H. Chen, B. Wang, L. Zheng, M. Wei, D. G. Evans, X. Duan, *J. Am. Chem. Soc.* **2016**, *138*, 6298.
- [9] S. Kato, M. Ammann, T. Huthwelker, C. Paun, M. Lampimäki, M.-T. Lee, M. Rothensteiner, J. A. Van Bokhoven, *Phys. Chem. Chem. Phys.* **2015**, *17*, 5078.
- [10] V. Golovanova, M. C. Spadaro, J. Arbiol, V. Golovanov, T. T. Rantala, T. Andreu, J. R. Morante, *Appl. Catal. B* **2021**, *291*, 120038.
- [11] N. M. Martin, F. Hemmingsson, A. Schaefer, M. Ek, L. R. Merte, U. Hejral, J. Gustafson, M. Skoglundh, A.-C. Dippel, O. Gutowski, M. Bauer, P.-A. Carlsson, *Catal. Sci. Technol.* **2019**, *9*, 1644.
- [12] M. Xiong, Z. Gao, Y. Qin, *ACS Catal.* **2021**, *11*, 3159.
- [13] V. Sharma, P. A. Crozier, R. Sharma, J. B. Adams, *Catal. Today* **2012**, *180*, 2.
- [14] S. Alayoglu, K. An, G. Melae, S. Chen, F. Bernardi, L. W. Wang, A. E. Lindeman, N. Musselwhite, J. Guo, Z. Liu, M. A. Marcus, G. A. Somorjai, *J. Phys. Chem. C* **2013**, *117*, 26608.
- [15] W. Karim, C. Spreafico, A. Kleibert, J. Gobrecht, J. Vandevondele, Y. Ekinci, J. A. Van Bokhoven, *Nature* **2017**, *541*, 68.
- [16] Y. Li, M. Kottwitz, J. L. Vincent, M. J. Enright, Z. Liu, L. Zhang, J. Huang, S. D. Senanayake, W. C. D. Yang, P. A. Crozier, R. G. Nuzzo, A. I. Frenkel, *Nat. Commun.* **2021**, *12*, 914.
- [17] W. Yuan, B. Zhu, K. Fang, X.-Y. Li, T. W. Hansen, Y. Ou, H. Yang, J. B. Wagner, Y. Gao, Y. Wang, Z. Zhang, *Science* **2021**, *371*, 517.
- [18] S. B. Vendelbo, C. F. Elkjær, H. Falsig, I. Puspitasari, P. Dona, L. Mele, B. Morana, B. J. Nelissen, R. Van Rijn, J. F. Creemer, P. J. Kooyman, S. Helveg, *Nat. Mater.* **2014**, *13*, 884.
- [19] S. W. Chee, T. Lunkenbein, R. Schlögl, B. R. Cuenya, *J. Phys. Condens. Matter* **2021**, *33*, 153001.
- [20] T. Ghosh, J. M. Arce-Ramos, W.-Q. Li, H. Yan, S. W. Chee, A. Genest, U. Mirsaidov, *Nat. Commun.* **2022**, *13*, 6176.
- [21] L. Artiglia, F. Orlando, K. Roy, R. Kopelent, O. Safonova, M. Nachttegaal, T. Huthwelker, J. A. Van Bokhoven, *J. Phys. Chem. Lett.* **2017**, *8*, 102.
- [22] A. Parastaev, V. Muravev, E. H. Osta, T. F. Kimpel, J. F. M. Simons, A. J. F. Van Hoof, E. Uslamin, L. Zhang, J. J. C. Struijs, D. B. Burueva, E. V. Pokochueva, K. V. Kovtunov, I. V. Koptyug, I. J. Villar-Garcia, C. Escudero, T. Altantzis, P. Liu, A. Béché, S. Bals, N. Kosinov, E. J. M. Hensen, *Nat. Catal.* **2022**, *5*, 1051.
- [23] C. Vogt, B. M. Weckhuysen, *Nat. Rev. Chem.* **2022**, *6*, 89.
- [24] W. Yuan, K. Fang, R. You, Z. Zhang, Y. Wang, *Acc. Mater. Res.* **2023**, *4*, 275.
- [25] M. Monai, K. Jenkinson, A. E. M. Melcherts, J. N. Louwen, E. A. Irmak, S. Van Aert, T. Altantzis, C. Vogt, W. Van Der Stam, T. Duchoň, B. Smíd, E. Groeneveld, P. Berben, S. Bals, B. M. Weckhuysen, *Science* **2023**, *380*, 644.
- [26] W. Albrecht, S. Van Aert, S. Bals, *Acc. Chem. Res.* **2021**, *54*, 1189.
- [27] B. Goris, S. Turner, S. Bals, G. Van Tendeloo, *ACS Nano* **2014**, *8*, 10878.
- [28] A. De Backer, L. Jones, I. Lobato, T. Altantzis, B. Goris, P. D. Nellist, S. Bals, S. Van Aert, *Nanoscale* **2017**, *9*, 8791.
- [29] T. Altantzis, I. Lobato, A. De Backer, A. Béché, Y. Zhang, S. Basak, M. Porcu, Q. Xu, A. Sánchez-Iglesias, L. M. Liz-Marzán, G. Van Tendeloo, S. Van Aert, S. Bals, *Nano Lett.* **2019**, *19*, 477.

- [30] S. Van Aert, K. J. Batenburg, M. D. Rossell, R. Erni, G. Van Tendeloo, *Nature* **2011**, 470, 374.
- [31] W. L. Vrijburg, J. W. A. Van Helden, A. J. F. Van Hoof, H. Friedrich, E. Groeneveld, E. A. Pidko, E. J. M. Hensen, *Catal. Sci. Technol.* **2019**, 9, 2578.
- [32] Z. Mao, P. G. Lustemberg, J. R. Rumptz, M. V. Ganduglia-Pirovano, C. T. Campbell, *ACS Catal.* **2020**, 10, 5101.
- [33] J. Gu, L. Jjiang, S. A. Ismail, H. Guo, D. Han, *Adv. Mater. Interfaces* **2023**, 10, 2201764.
- [34] H. Frey, A. Beck, X. Huang, J. A. Van Bokhoven, M. G. Willinger, *Science* **2022**, 376, 982.
- [35] A. Beck, X. Huang, L. Artiglia, M. Zabilskiy, X. Wang, P. Rzepka, D. Palagin, M.-G. Willinger, J. A. Van Bokhoven, *Nat. Commun.* **2020**, 11, 3220.
- [36] B. Goris, M. Meledina, S. Turner, Z. Zhong, K. J. Batenburg, S. Bals, *Ultramicroscopy* **2016**, 171, 55.
- [37] R. Ciancio, R. E. Dunin-Borkowski, E. Snoeck, M. Kociak, R. Holmestad, J. Verbeeck, A. I. Kirkland, G. Kothleitner, J. Arbiol, *Microsc. Microanal.* **2022**, 28, 2900.